






Letters

On the Dynamics of Inherent Balancing of Modular Multilevel DC–AC–DC Converters

Xin Xiang , *Member, IEEE*, Yunjie Gu , *Senior Member, IEEE*, Kaiwen Chen ,
Alessandro Astolfi , *Fellow, IEEE*, and Timothy C. Green , *Fellow, IEEE*

Abstract—Modular multilevel dc–ac–dc converters (MMDACs) serve as an enabler for dc distribution systems. The modular multilevel structure enables flexible voltage transforms, but raises issues over balancing of the submodule (SM) capacitor voltages. This letter focuses on the dynamics of inherent balancing of MMDACs under circulant modulation. We provide an invariance-like result using a variant of Barbalat’s Lemma and prove that the SM capacitor voltages converge to the kernel of the circulant switching matrix, which is the intersection of the invariant sets for each switching state. We further interpret the balancing dynamics as a permuted linear time-invariant system and prove that the envelop of the balancing trajectories is governed by the eigenvalues of the permuted state-transition matrix. This result extends previous full-rank criterion for inherent balancing in a steady state and provides new insight into the dynamic behavior of MMDACs.

Index Terms—Barbalat’s lemma, circulant modulation, inherent balancing, invariance principle, permuted linear time-invariant (LTI) systems.

I. INTRODUCTION

MODULAR multilevel dc–ac–dc converters (MMDACs) [1]–[3] show promise as interconnection equipment in dc distribution systems between medium-voltage dc (MVdc) networks and low-voltage dc (LVdc) layers [4]. Circulant modulation has been proposed as an extension of the classical phase-shift modulation [5], which provides inherent balancing of capacitor voltages in the submodules (SM) of the MMDACs [6]. Inherent voltage balancing of SM capacitors is highly attractive for MMDACs. It equalizes voltage stress, current stress, switching frequency, and power losses across SMs, thus reducing the need for safety margins in the design. It also reduces

the computational burden on the control hardware by obviating the real-time sorting and re-ordering of SM switching, which is inevitable in noninherent balancing schemes [7]. Common sorting algorithms (e.g., the bubble sorting) has the time complexity of $O(n^2)$ where n is the number of SMs, so fast and expensive field programmable gate arrays are usually needed in the central controller for real-time sorting. The inherent balancing schemes, in contrast, can be fully distributed to local controllers in each SMs and the corresponding time complexity is $O(1)$. This not only enables slower and cheaper control chips to be used but also makes the control system has very high scalability for the number of SMs, which is ever increasing to handle higher voltage. Therefore, inherent voltage balancing creates cost-effective solutions for both the power converter and its control system.

For the aforementioned reasons the capability of inherent voltage balancing has recently attracted much attention. Inherent balancing has been demonstrated to occur for various cases of MMDACs [8], [9]. In [10], a generalized full-rank criterion and coprime criterion to guarantee inherent balancing have been established. However, all existing investigations are limited to steady-state conditions, whereas the analysis under dynamic conditions has not been undertaken yet. In particular, it is unclear whether the capacitor voltages converge or otherwise to the balancing point in response to disturbances.

To fill this gap, this letter investigates the dynamics of inherent balancing for MMDACs. In particular, we provide an invariance-like result using a variant of Barbalat’s Lemma and prove that the SM capacitor voltages converge to the kernel of the circulant switching matrix, which is the intersection of the invariant sets for each switching state. We further interpret the balancing dynamics as a permuted linear time-invariant system (LTI) and prove that the envelop of the balancing trajectories is governed by the eigenvalues of the permuted state-transition matrix. This result extends the previous full-rank criterion for steady-state inherent balancing [10], and also reveals the linkage between the dynamic behavior of MMDACs and the geometric structure of the circulant modulation matrix. The methodology established in this letter is generally suitable for a variety of MMDACs, including dual-active-bridge (DAB)-based MMDACs and LLC-based MMDACs, and could be further extended to general modular multilevel converters (MMCs).

Manuscript received May 8, 2020; revised June 2, 2020; accepted June 6, 2020. Date of publication June 9, 2020; date of current version September 4, 2020. This work was supported by the Engineering and Physical Sciences Research Council of U.K. (EPSRC) under Awards EP/S000909/1 and EP/T001623/1. (Corresponding author: Yunjie Gu.)

The authors are with the Department of Electrical and Electronic Engineering, Imperial College London, London SW7 2BU, U.K. (e-mail: x.xiang14@imperial.ac.uk; yunjie.gu@imperial.ac.uk; kaiwen.chen16@imperial.ac.uk; a.astolfi@imperial.ac.uk; t.green@imperial.ac.uk).

Color versions of one or more of the figures in this article are available online at <https://ieeexplore.ieee.org>.

Digital Object Identifier 10.1109/TPEL.2020.3001431

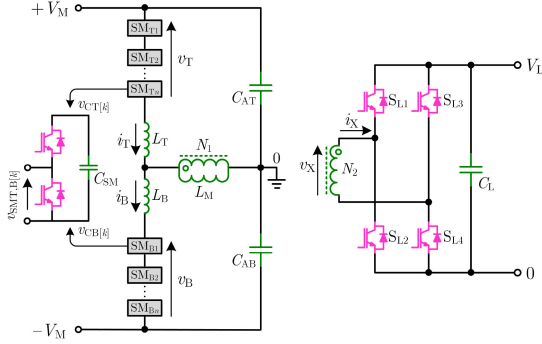


Fig. 1. Representative topology of DAB-based MMDAC.

II. MMDACs WITH CIRCULANT MODULATION

The detailed operating principles of MMDACs with circulant modulation have been described in the literature, see e.g., [8] and [10]. The key points are summarized for convenience. A representative topology of a DAB-based MMDAC is illustrated in Fig. 1. Other types of MMDACs share similar stack topologies and operational principles.

Taking the top stack (n half-bridge SMs in total) as an example, during each positive stage, of duration T_P , there are m ($1 \leq m < n$) SM capacitors switched into the conduction path (which is called “switched in” below in short), whereas the remaining $n - m$ SMs are bypassed. In this stage, the top stack voltage v_T is smaller than the MVdc link voltage $+V_M$, which results in a positive voltage (with respect to the neutral point, node 0) at the bottom end of the stack at the connection to the arm inductor L_T . During each negative stage, of duration T_N , all the n SMs are switched in, leading to a negative voltage at the bottom of the stack with respect to the neutral point. We set $T_P = T_N$; thus, a symmetric square-wave is applied at the connection to L_T . The bottom stack is switched in a complementary fashion to the top stack to produce a similar square-wave at the connection to L_B . Together they form the primary-side bridge voltage. The secondary-side bridges S_{L1} to S_{L4} generate another square-wave, which is given a phase shift φ , as in the classical DAB, in order to control the current flow.

Circulant modulation is used to select which specific SMs are switched in during each stage, which is governed by the turntables in Fig. 2. We still take the top stack as an example, as shown in Fig. 2(a). The outer layer of the turntable represents all SMs in the stack. The middle layer colored blue indicates which n SMs are switched in during the negative stages, and the inner layer colored red indicates which m SMs are switched in during the positive stages. The outer and middle layers are fixed, whereas the inner layer rotates clockwise by one-step in

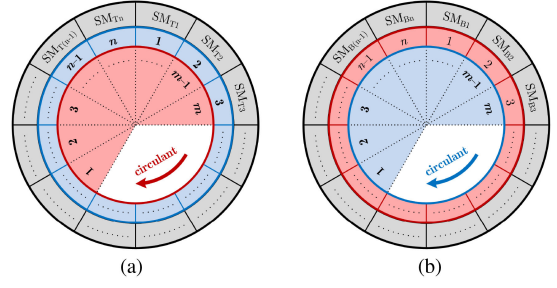


Fig. 2. Circulant modulation. (a) Top stack. (b) Bottom stack.

each base cycle; hence, different SMs are switched in at different base cycles, but all are used equally for an entire circulant cycle. The turntable for the bottom stack works in complement to that of the top stack, as shown in Fig. 2(b). It takes n steps for the turntables to complete one cycle, so the circulant cycle T_{CC} is n times the base cycle, i.e., $T_{CC} = nT_{BC}$.

III. DYNAMICS OF INHERENT BALANCING

A key advantage of circulant modulation is that it ensures inherent balancing of each SMs. The static balancing mechanism has been investigated in [10]. We here extend the investigation to the dynamic balancing properties.

A. Mathematical Formulation

We first establish the mathematical formulation to describe the balancing dynamics. The state equations of the DAB-based MMDAC are given in (1) shown at the bottom of this page. In these equations, L_T and L_B denote the value of arm inductances, R_T and R_B denote the value of their resistances, and i_T and i_B describe the currents through each arm. The total resistance of the transformer seen from the primary side is represented by R_X . Each SM has a capacitor of value C_{SM} , and v_{CT} and v_{CB} are column vectors describing the voltages across each capacitor. The voltages at the MVdc and LVdc terminals, V_M and V_L , respectively, are assumed to be constant.

The operation of the converter is governed by the switching signals: s_T and s_B are n -dimensional row vectors of the states of the SMs in the top and bottom stacks and s_L is a scalar determining the state of the secondary-side bridge. The values of s_T , s_B , and s_L are defined as follows:

$$\begin{aligned} s_{T[k]} &= 1 : \text{SM}_{T_k} \text{ is switched in, } s_{T[k]} = 0 : \text{otherwise} \\ s_{B[k]} &= 1 : \text{SM}_{B_k} \text{ is switched in, } s_{B[k]} = 0 : \text{otherwise} \\ s_L &= 1 : S_{L1}, S_{L4} \text{ are ON, } s_L = -1 : S_{L2}, S_{L3} \text{ are ON} \end{aligned} \quad (2)$$

$$\underbrace{\begin{pmatrix} L_T \dot{i}_T \\ L_B \dot{i}_B \\ C_{SM} \dot{v}_{CT} \\ C_{SM} \dot{v}_{CB} \end{pmatrix}}_{E \dot{x}} = \underbrace{\begin{pmatrix} -R_T - R_X & R_X & -s_T & 0 \\ R_X & -R_B - R_X & 0 & -s_B \\ s_T^\top & 0 & 0 & 0 \\ 0 & s_B^\top & 0 & 0 \end{pmatrix}}_A \underbrace{\begin{pmatrix} i_T \\ i_B \\ v_{CT} \\ v_{CB} \end{pmatrix}}_x + \underbrace{\begin{pmatrix} 1 & -s_L \\ 1 & +s_L \\ 0 & 0 \\ 0 & 0 \end{pmatrix}}_B \underbrace{\begin{pmatrix} V_M \\ \frac{N_1}{N_2} V_L \end{pmatrix}}_u. \quad (1)$$

where the subscript $[k]$ identifies the k th element of a vector. The switching signal s_L switches between ± 1 every base cycle T_{BC} with a duty cycle of 0.5. The switching signal s_T switches between s_P and s_N in synchronism with s_L (with a phase angle in between to control the current flow), and the switching signal s_B switches between s_N and s_P in complement to s_T . s_N is an all-one vector and s_P rotates among s_1, s_2, \dots, s_n , which together form the circulant matrix S

$$S = \begin{pmatrix} s_1 \\ s_2 \\ \vdots \\ s_n \end{pmatrix} = \begin{pmatrix} \overbrace{1 & 1 & \cdots & 1 & 1}^{m} & \overbrace{0 & 0 & \cdots & 0 & 0}^{m-n} \\ 0 & 1 & \cdots & 1 & 1 & 1 & 0 & \cdots & 0 & 0 \\ & & \vdots & & & & & \vdots & & \\ 1 & 1 & \cdots & 1 & 0 & 0 & 0 & \cdots & 0 & 1 \end{pmatrix}. \quad (3)$$

This circulant matrix is introduced to facilitate the mathematical formulation of the circulant modulation described in Section II.

The state equations (1) can be rewritten as

$$E\dot{x} = Ax + Bu \quad (4)$$

where the matrix

$$E = \text{diag}(L_T, L_B, C_{SM}, C_{SM}) \quad (5)$$

is associated to the energy storage components in the system and A , B , x , and u are defined in (1). Equation (4) is a linear time-periodic (LTP) system and its solution is of the form

$$x = \tilde{x} + \hat{x} \quad (6)$$

where \tilde{x} is a periodic vector function of time describing the steady-state solution and \hat{x} is a nonperiodic vector function of time describing the transients [11]. It has been proved in [10] that \tilde{x} is unique if and only if S is full rank. We further show that the dynamic behavior and convergence properties of \hat{x} are also determined by S .

Removing the steady state \tilde{x} from (4), we get the transient state equation for \hat{x}

$$E\dot{\hat{x}} = A\hat{x}. \quad (7)$$

This is a time-varying so the conventional LTI system theory is not applicable. In the following sections, we take two different routes to investigate the properties of (7) and thereby reveal the mechanisms and properties of the dynamic balancing.

B. Energy-Based Method

Define the energy function of the system (7) as $H(\hat{x}) = \frac{1}{2}\hat{x}^\top E\hat{x}$ and note that its time-derivative along the trajectories is negative semidefinite, that is

$$\dot{H}(\hat{x}) = \hat{x}^\top A\hat{x} = -\hat{i}_T^2 R_T - \hat{i}_B^2 R_B - (\hat{i}_T - \hat{i}_B)^2 R_X \leq 0. \quad (8)$$

According to Lyapunov's theorem, if $\dot{H}(\hat{x})$ is strictly negative definite, the total energy of the system keeps decrease over time so the states eventually converge to the equilibrium where the energy is the lowest. In our case, however, $\dot{H}(\hat{x})$ is only negative semidefinite so there might exist limit cycles of the trajectories along which $\dot{H}(\hat{x}) \equiv 0$. Such limit cycles can be assessed by the invariant set of the system according to LaSalle's invariance

principle, but in the preset case, A is time varying; hence, the classical invariance method is not directly applicable. We seek instead an invariance-like result using a variant of Barbalat's Lemma [12], [13]. To address the discontinuities of A at the time of switching, we need to slightly modify Barbalat's Lemma as follows.

Definition 1 (Uniform one-sided continuity): A function $f: \mathbb{D} \rightarrow \mathbb{R}^n$, where $\mathbb{D} \subseteq \mathbb{R}$, is called uniformly one-sided continuous if for all $\epsilon > 0$ there exists $\delta > 0$ such that for all $t_0 \in \mathbb{D}$, we have either of the following conditions:

- 1) $|f(t) - f(t_0)| < \epsilon$, for all $t \in (t_0 - \delta, t_0]$
- 2) $|f(t) - f(t_0)| < \epsilon$, for all $t \in [t_0, t_0 + \delta)$.

Lemma 1 (A variant of Barbalat's Lemma): Suppose $f'(t)$ is uniformly one-sided continuous on $[0, \infty)$ and integrable on any closed subinterval of $[0, \infty)$. Let $f(t) = \int_0^t f'(\tau) d\tau + f_0$. If $\lim_{t \rightarrow \infty} f(t)$ exists and is finite, then $\lim_{t \rightarrow \infty} f'(t) = 0$.

Proof: We prove the claim by contradiction in the same spirit as the proof in [12]. Suppose $\lim_{t \rightarrow \infty} f'(t) \neq 0$. Then, there exists $\epsilon > 0$ and a monotonic increasing sequence $\{t_k\}$ with $\lim_{k \rightarrow \infty} t_k = +\infty$, such that $|f'(t_k)| \geq \epsilon$ for all $n \in \mathbb{N}$. Since f' is uniformly one-sided continuous, for such an ϵ there exists $\delta > 0$ such that, for any $k \in \mathbb{N}$, $|f'(t) - f'(t_k)| \leq \frac{\epsilon}{2}$ for $t \in (t_k - \delta, t_k]$ or for $t \in [t_k, t_k + \delta)$. As a result, either

$$|f(t_k) - f(t_k - \delta)| = \left| \int_{t_k - \delta}^{t_k} f'(t) dt \right| \geq \frac{\epsilon\delta}{2} \quad (9)$$

or

$$|f(t_k + \delta) - f(t_k)| = \left| \int_{t_k}^{t_k + \delta} f'(t) dt \right| \geq \frac{\epsilon\delta}{2}. \quad (10)$$

Hence, we conclude that $f(t)$ does not converge. This is a contradiction. Therefore $\lim_{t \rightarrow \infty} f'(t) = 0$. ■

It is clear that H is bounded and so is \hat{x} . Therefore, $\dot{\hat{x}} = E^{-1}A\hat{x}$ is also bounded, implying that \hat{x} is uniformly continuous. A is not continuous due to the switching action, but is uniformly one-sided continuous if we define its value at the switching point to be its left-limit. It follows that $\dot{\hat{x}}$ and \dot{H} are uniformly one-sided continuous. As a result

$$\lim_{t \rightarrow \infty} H < \infty \implies \lim_{t \rightarrow \infty} \dot{H} = 0 \stackrel{(8)}{\implies} \lim_{t \rightarrow \infty} \hat{i}_T = \lim_{t \rightarrow \infty} \hat{i}_B = 0 \quad (11)$$

and

$$\lim_{t \rightarrow \infty} \hat{i}_T = 0 \implies \lim_{t \rightarrow \infty} \dot{\hat{i}}_T = 0 \stackrel{(1)}{\implies} \lim_{t \rightarrow \infty} s_T \hat{v}_{CT} = 0. \quad (12)$$

We now define an auxiliary variable $s_k \hat{v}_{CT}$ and show that it also converges. As $t \rightarrow \infty$, $\hat{v}_{CT} = C_{SM}^{-1} s_T^\top \hat{i}_T$ converges, hence the variation of \hat{v}_{CT} and $s_k \hat{v}_{CT}$ in a finite time interval converges to 0. Under the circulant modulation, $s_k \hat{v}_{CT}$ equals $s_T \hat{v}_{CT}$ periodically, hence

$$\lim_{t \rightarrow \infty} s_T \hat{v}_{CT} = 0 \implies \lim_{t \rightarrow \infty} s_k \hat{v}_{CT} = 0, \text{ for all } k = 1, 2, \dots, n. \quad (13)$$

Rewriting (13) in a matrix form yields

$$\lim_{t \rightarrow \infty} S \hat{v}_{CT} = 0 \quad (14)$$

which implies that \hat{v}_{CT} converges to the kernel of S , and this conclusion also applies to \hat{v}_{CB} .

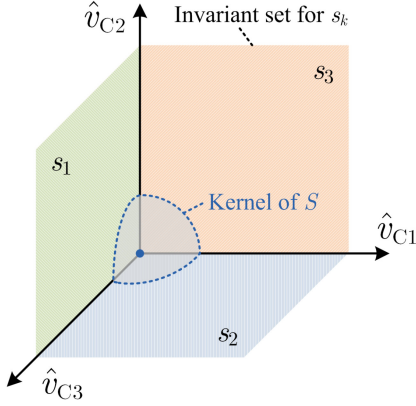


Fig. 3. Dissipation of the system drives the state trajectories to the kernel of the switching matrix S , which is the intersection of the invariant sets for different switching states $s_{k=1,2,\dots,n}$.

If S is full rank, its kernel contains only the zero vector, which means that SMs are uniformly balanced dynamically. Otherwise, the dynamic balancing splits and the SM voltages may settle at different points for different groups depending on the structure of the kernel. As a result, we have extended the full-rank criterion [10] to balancing dynamics and we have shown that the kernel of S describes the invariant set of the trajectories of the system.

To aid understanding, the reasoning developed earlier is illustrated in Fig. 3. The SM capacitor voltages $\hat{v}_{C[1]}, \hat{v}_{C[2]}, \dots, \hat{v}_{C[n]}$ (we drop the subscript T and B for ease of notation) form a vector in \mathbb{R}^n and the invariant set is a subspace of \mathbb{R}^n with zero dissipation, where the net voltages applied on the arm inductors are zero and, therefore, neither currents nor conduction losses are induced in the inductor windings. For different switching state $s_{k=1,2,\dots,n}$, the invariant set is different, and the final invariant set of the trajectories of the system is their intersection, which is the kernel of S . The dissipation in the system drives \hat{v}_{SM} to the kernel of S and forces it to remain there.

C. Permuted LTI System

The energy-based method assesses the convergence range and condition of the balancing dynamics, but does not shed light on the detailed dynamic process. We now fill this gap by evaluating the state transition matrix cycle-by-cycle. For each of the switching state, (7) describes an LTI system and its solution can be described via the state-transition matrix $\Phi = e^{E^{-1}Ah}$, where h is the dwell time. Every base cycle contains two switching states due to the commutation between the positive and negative stage; hence, the state-transition matrix for the k th base cycle is given by

$$\Phi_k^B = e^{E^{-1}A_k^N T_N} e^{E^{-1}A_k^P T_P} \quad (15)$$

in which A_k^P and A_k^N represent the A matrix in the positive and negative stage of the k th base cycle, respectively. We then have $\hat{x}_k = \Phi_k^B \hat{x}_{k-1}$ where \hat{x}_k is the value of \hat{x} at the end of the k th base cycle and \hat{x}_0 is the initial state. The overall state-transition

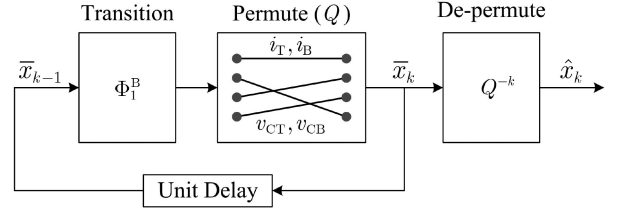


Fig. 4. Balancing dynamics Φ_k interpreted as a permuted LTI system.

matrix from the initial state to the state in the k th base cycle is

$$\Phi_k = \Phi_k^B \dots \Phi_3^B \Phi_2^B \Phi_1^B, \text{ yielding } \hat{x}_k = \Phi_k \hat{x}_0. \quad (16)$$

The matrix Φ_k governs the overall balancing dynamics and it has very interesting properties. It is clear that Φ_k^B is periodic, that is, $\Phi_k^B = \Phi_{n+k}^B$. Using this property, we rearrange (16) as

$$\Phi_k = \Phi_{V\alpha} \Phi_C^\beta \quad (17)$$

in which

$$\Phi_{V\alpha} = \Phi_{B\alpha} \dots \Phi_{B2} \Phi_{B1}, \quad \Phi_C = \Phi_{Bn} \dots \Phi_{B2} \Phi_{B1} \quad (18)$$

$\beta = \lfloor k/n \rfloor$ and $\alpha = k - n\beta$. $\Phi_{V\alpha}$ is again a periodic matrix governing the state variation inside a circulant cycle, whereas Φ_C^β governs the state transition over β circulant cycles and, hence, determines the overall balancing dynamics.

To further simplify Φ_k , we make use of the following recursive relationship intrinsic to the circulant modulation:

$$A_k^P = Q^\top A_{k-1}^P Q, \quad A_k^N = Q^\top A_{k-1}^N Q \quad (19)$$

in which

$$Q = \text{blkdiag}(1, 1, P, P) \quad (20)$$

and P is the n th-order circulant permutation matrix serving as a circulant shift operator on the switching vector, that is

$$P = \begin{pmatrix} 0 & 1 & \dots & 0 \\ 0 & 0 & \ddots & 0 \\ 0 & 0 & \dots & 1 \\ 1 & 0 & \dots & 0 \end{pmatrix}. \quad (21)$$

Substituting (19) into (16) and making use of the facts that Q^\top equals Q^{-1} and that Q commutes with E^{-1} yield

$$\Phi_k^B = Q^{-1} \Phi_{k-1}^B Q = Q^{-(k-1)} \Phi_1^B Q^{k-1} \quad (22)$$

hence

$$\Phi_k = Q^{-k} (Q \Phi_1^B)^k. \quad (23)$$

Equations (23) and (17) are equivalent and we can easily see that

$$\Phi_C = (Q \Phi_1^B)^n \text{ or equivalently } \Phi_C^{\frac{1}{n}} = Q \Phi_1^B. \quad (24)$$

Nonetheless, (23) provides a more insightful interpretation on the dynamics of the system, which is named the permuted LTI system, as illustrated in Fig. 4. In this interpretation, the circulant modulation is reflected by the permutation of the state $\bar{x}_k =$

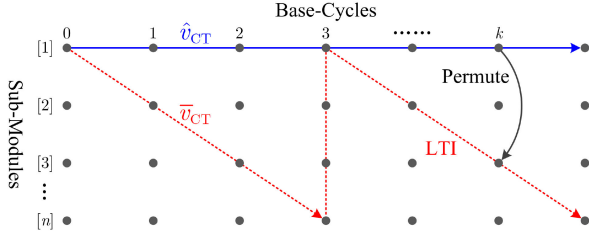


Fig. 5. Illustration of the state-transition mechanism of the permuted LTI system.

$Q^k \hat{x}_k$, instead of the variation of the transition matrix Φ_k^B , which leads to the LTI system

$$\bar{x}_k = Q\Phi_1^B \bar{x}_{k-1} \quad (25)$$

in which $Q\Phi_1^B$ is called the permuted state-transition matrix. Then, the permuted state \bar{x}_k is depermuted to retain the original state \hat{x}_k , that is

$$\hat{x}_k = Q^{-k} \bar{x}_k. \quad (26)$$

This mechanism is further illustrated in Fig. 5. The solid blue arrow represents the dynamics of the original states \hat{x} , and the dashed red arrow represents the dynamics of the permuted states \bar{x} (we take the capacitor voltages of the top stack as an example). The state-transition along the dashed red arrow is that of an LTI system, which can be depermuted to retain the original state as indicated by the solid blue arrow.

The depermuted transformation Q^{-k} is also periodic, that is, $Q^{-k} = Q^{n-k}$. It only changes the order of the state variables, whereas the envelop of the overall state trajectory is governed by the matrix $Q\Phi_1^B$ alone, and more specifically, by its eigenvalues. Such eigenvalues can be calculated numerically and the dominant eigenvalue(s) can be used to quantify the balancing dynamics. On the other hand, we can estimate the qualitative distribution of the eigenvalues according to the switching matrix S and the corresponding invariant set of the system. If S is full-rank, all eigenvalues of $Q\Phi_1^B$ lie within the open unit disc on the complex plane, meaning that all trajectories converge to zero. Otherwise, there is at least one eigenvalue on the unit circle and the eigenspace of such eigenvalues is the kernel of

$$W = \text{blkdiag}(1, 1, S, S) \quad (27)$$

which establishes the linkage between the invariant set of the original system and the permuted LTI system.

D. Sensitivity Analysis

We now analyze the sensitivity of the balancing dynamics to converter parameters. The norm of the dominant eigenvalues of $Q\Phi_1^B$ determines the settling time of the balancing process and is, therefore, used to quantify the sensitivity. The dominant eigenvalues are calculated for different n and C_{SM} and their norm are plotted in Fig. 6. It is clear that the norm of the dominant eigenvalues increases with larger n and C_{SM} but are strictly smaller than one for all cases. This indicates that the balancing process becomes slower with more SMs and higher SM capacitances but remains converging.

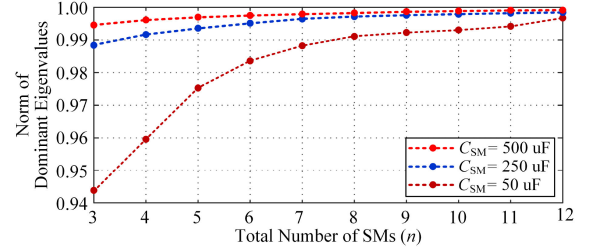


Fig. 6. Norm of the dominant eigenvalues for a variety of n and C_{SM} . In all cases m is set as $m = n - 1$. The parameters unspecified here are listed in Table I.

TABLE I
CIRCUIT PARAMETERS OF DOWN-SCALED PROTOTYPE

Parameters	Descriptions	Values
P	Maximum Operation Range	± 500 W
$\pm V_M$	MVDC link voltage	± 350 V
V_L	LVDC link voltage	20 V
L_T, L_B	Arm inductance	350 μ H
R_T, R_B	Resistance of arm inductor	0.7 Ω
$\frac{N_1}{N_2}$	Internal transformer turns-ratio	2.5:1
R_X	Total resistance of transformer	6.7 Ω
T_{CC}	Circulant cycle	4/3000 s
T_{BC}	Base cycle	1/3000 s
n	SM number in top and bottom stack	4
C_{SM}	SM capacitance	50 μ F \pm 10 μ F

We then investigate the impact of the capacitance variation among SMs. In such cases, the permutation relationship and the permuted state-transition matrix $Q\Phi_1^B$ no longer hold strictly, but the invariance set of the system and the circulant-cycle state transition matrix (17) are still valid. The impact of capacitance variation among SMs can thus be quantified by the difference of the dominant eigenvalues of $Q\Phi_1^B$ and $\Phi_C^{\frac{1}{n}}$ according to (24). Based on the parameters in Table I, we change the capacitance of one of the four SMs in the top stack by +20%, and change another one in the bottom stack by -20%. The corresponding norm of the dominant eigenvalues of $Q\Phi_1^B$ and $\Phi_C^{\frac{1}{n}}$ are 0.9575 and 0.9597, respectively, whose difference is almost negligible. This implies that the balancing dynamics is not sensitive to capacitance variation among SMs.

On the other hand, C_{SM} and its variation among SMs do have significant impact on the ripple of the SM capacitor voltage, which is not explicitly taken into account by $Q\Phi_1^B$ or Φ_C since the voltage ripples within each cycle are not sampled in these formulations. The voltage ripple does not affect the balancing dynamics and is invisible to the MVdc and LVdc terminals. However, it may have significant impacts on the reliability of the capacitor and power devices and, therefore, important in engineering design. The SM capacitor voltage variation is caused by the current through the stack when the SM is switched in. For each SM, it is switched in for consecutive m base cycles (called period one) and then alternates between being switched in and being bypassed for $n - m$ base cycles (called period two).

In these two periods, the SM capacitor charge or discharge in opposite directions, so the overall voltage ripple can be estimated by the accumulated charge in either period. We use period one to do the calculation. Taking an SM in the top stack as example (the bottom stack is the same), the overall voltage ripple is

$$\Delta V = \frac{1}{2} \int_0^{mT_{BC}} \frac{i_T}{C_{SM}} = \frac{1}{2} \int_0^{mT_{BC}} \frac{I_M}{C_{SM}} = \frac{mI_M T_{BC}}{2C_{SM}} \quad (28)$$

where I_M is the dc current at the MVdc terminal. In (28), we make use of the fact that the ac component in i_T alternate every base cycle and, therefore, does not generate voltage variation during the whole m base cycles. As a result, the voltage ripple is proportional to the dc current and the corresponding power rating of the system. The SM capacitance C_{SM} should be designed accordingly considering the manufacturing tolerance to keep the maximum ripple within the reliability constraint. It is also notable in (28) that the voltage ripple ΔV has a multiplier m (number of SMs switched in at each positive stage) which is usually proportional to the voltage rating on the primary side. This is not a problem for medium voltage applications where m is usually below ten, but might become an issue for high-voltage applications where m can be as high as several hundred. This problem can be solved by extending the circulant modulation into each base cycles (that is, $T_{CC} = T_{BC}$), but this is beyond the scope of this letter.

IV. EXPERIMENTAL VALIDATION

To validate the theoretical analysis for the dynamics of inherent balancing in MMDACs, experiments were conducted on a down-scaled prototype of the DAB-based MMDAC with the circuit parameters given in Table I. The controller used in this down-scaled prototype is a basic microcontrol unit, TMS320F28335. A practical square-wave internal transformer could be designed according to the principles in [14] and the transformer in this prototype is set to operate at the medium frequency of 3 kHz ($T_{BC} = 1/3000$ s) after consideration of the practical applications of MMDACs [15]. A full-rank circulant matrix S with $m = 3$ and $n = 4$ (see equation (3)) is used for demonstration, that is, each stack of the converter switches three SM capacitors into the circuit for positive stages and switches in four SM capacitors for negative stages to create the square-wave on the primary side.

To begin with, the start-up test was conducted. The dynamic behavior of the top stack is illustrated in Fig. 7 with each SM output voltage displayed in Fig. 7(a) and each SM capacitor voltage displayed in Fig. 7(b). The converter operation starts at 40 ms. It can be observed that the SM capacitor voltages are charged from 0 V at 40 ms and all of them are inherently balanced at 100 V at 180 ms, indicating that the converter has finished the start-up process and entered steady-state operation. To provide a broader validation, another dynamic start-up experiment was conducted but with $m = 1$ and $n = 4$ and the results obtained are shown in Fig. 8. It is clear that the SM capacitor voltages are still inherently balanced but with a minor difference in the transient trajectories compared to the case of $m = 3$ and $n = 4$ in Fig. 7. These results verify the inherent balancing capability

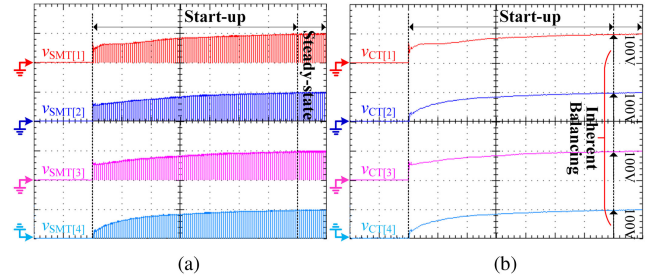


Fig. 7. Experimental results of dynamic start-up process with operation case of $m = 3$ and $n = 4$ (time-scale 20 ms/div). (a) SM output voltages $v_{SMT[k]}$ (100 V/div). (b) SM capacitor voltages $v_{CT[k]}$ (100 V/div).

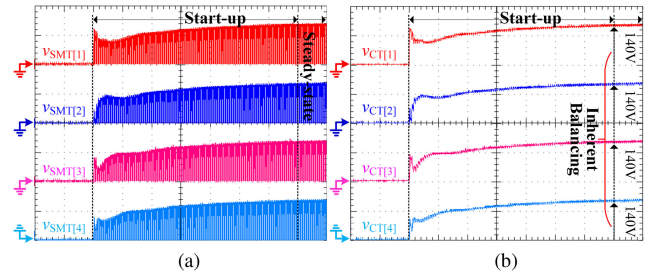


Fig. 8. Experimental results of dynamic start-up process with another operation case of $m = 1$ and $n = 4$ (time-scale 20 ms/div). (a) SM output voltages $v_{SMT[k]}$ (100 V/div). (b) SM capacitor voltages $v_{CT[k]}$ (100 V/div).

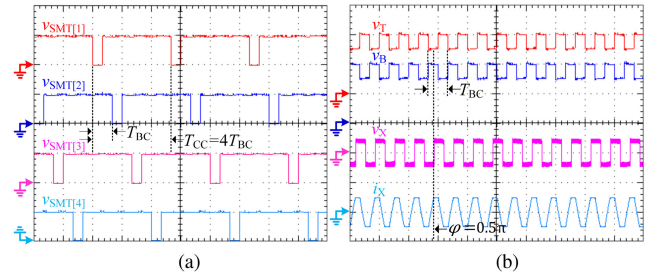


Fig. 9. Experimental results of steady-state operation for maximum positive power operation (time-scale 500 μ s/div). (a) SM output voltages $v_{SMT[k]}$ (100 V/div). (b) Stack voltages v_T and v_B (200 V/div), transformer voltage v_X (50 V/div), and current i_X (100 A/div).

of the circulant modulation during the dynamic start-up process for a wide range of voltage conversion ratios.

The waveforms of the SM output voltages, $v_{SMT[k]}$, in the steady-state operation of Fig. 7 are shown in an expanded view in Fig. 9(a). There are always three SMs switched into the circuit for each positive stage and there is a circulant sequence among them, as expected from the turntable in Fig. 2. The voltage generated by the top stack v_T , shown in Fig. 9(b), is seen to be complimentary to that of the bottom stack v_B . They both appear at an angle φ with respect to the secondary-side transformer voltage v_X to control the current flow i_X as in the classical DAB converter [2]. The phase-shift angle in this test is set at 0.5π to obtain maximum positive power flow. The converter operation under maximum negative power flow is very similar except that the phase-shift angle φ and the current i_X are opposite.

The experimental results for the load step response are shown in Fig. 10. In Fig. 10(a), the phase-shift angle is set at 0.5π initially for full power operation and then decreased to 0.25π

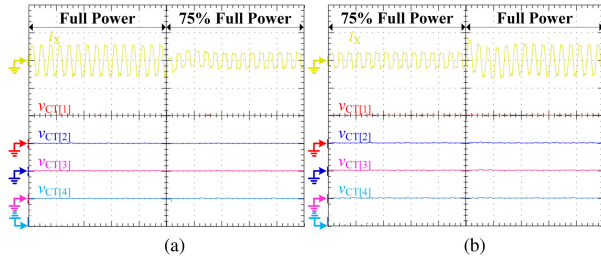


Fig. 10. Experimental results for the load step response (time-scale 1 ms/div): transformer current i_x (100 A/div) and SM capacitor voltages $v_{CT[k]}$ (100 V/div). (a) From full power to 75% power. (b) From 75% power to full power.

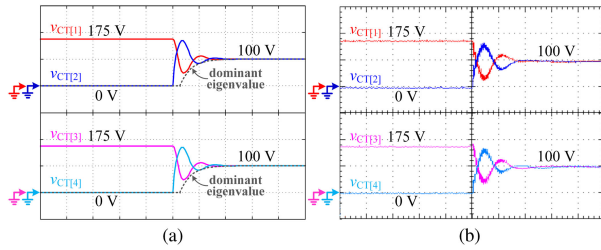


Fig. 11. Comparison between theoretical results and experimental results of a dynamic transient-change process from an unbalance state to the balance state (time-scale 20 ms/div). (a) Theoretical results for SM capacitor voltages $v_{CT[k]}$ (100 V/div). (b) Experimental results for SM capacitor voltages $v_{CT[k]}$ (100 V/div).

halfway through the observation period for 75% full power operation. The reverse process is provided in Fig. 10(b). It can be observed that the transformer current experience a step change in amplitude (with a minor overshoot) but all the SM capacitor voltages are almost not affected, which indicates that the balancing dynamics is not sensitive to load conditions. The SM capacitor voltage ripples are proportional to load current and, therefore, also experience a step change in amplitude, but the voltage ripples are rather small compare to the scale of the voltage probes used in the experiment and, thus, almost invisible in Fig. 10.

Finally, to verify the analysis of the dynamics of inherent balancing, the trajectories of the SM capacitor voltages $v_{CT[k]}$ from a unbalance state to the balance state, are plotted in detail in Fig. 11. The experimental results in Fig. 11(b) are compared with the theoretical results in Fig. 11(a). The envelopes of the trajectories are also plotted in Fig. 11(a) (dashed lines) according to the dominant pair of eigenvalues of the permuted state-transition matrix $Q\Phi_1^B$, namely, $\lambda = -0.9559 \pm 0.0841i$. These waveforms show great agreement with each other in terms of amplitude, oscillation frequency, and convergence time. All of the SM capacitors are inherently balanced to 100 V, which is the kernel of the full-rank switching matrix S with 100 V offset representing the steady state. It is worth noting that the high-frequency ripples seen in the transient process in Fig. 11(b) are caused by the stack voltage variations in different positive and negative stages within one circulant cycle. The unbalanced SM capacitor voltages during the transient lead to larger stack voltage variations and, thus, higher arm current ripples than those during the steady-state. The theoretical model does not

reflect this very fast dynamics within each base cycle, so the high-frequency ripples do not appear in the theoretical results of Fig. 11(a).

V. CONCLUSION

This letter has established an analytical framework to investigate the balancing dynamics of MMDACs. Using a variant of Barbalat's Lemma, we have proven that the capacitor voltages of all SMs converge to the kernel of the circulant matrix S , which is essentially the intersection of the invariant sets associated to every switching state. The SM capacitor voltages balance uniformly if and only if the kernel of S contains only the zero vector. The envelop of the balancing trajectory is governed by the eigenvalues of the permuted state-transition matrix. These conclusion extended the full-rank criterion established for steady-state balancing and provided further insight into the dynamic behavior of MMDACs. This approach has the potential to be generalized to other MMCs.

REFERENCES

- [1] S. Shao, M. Jiang, J. Zhang, and X. Wu, "A capacitor voltage balancing method for a modular multilevel DC transformer for DC distribution system," *IEEE Trans. Power Electron.*, vol. 33, no. 4, pp. 3002–3011, Apr. 2018.
- [2] B. Zhao, Q. Song, J. Li, Y. Wang, and W. Liu, "Modular multilevel high-frequency-link DC transformer based on dual active phase-shift principle for medium-voltage DC power distribution application," *IEEE Trans. Power Electron.*, vol. 32, no. 3, pp. 1779–1791, Mar. 2017.
- [3] S. Shao *et al.*, "A modular multilevel resonant DC-DC converter," *IEEE Trans. Power Electron.*, vol. 35, no. 8, pp. 7921–7932, Aug. 2020.
- [4] Y. Gu *et al.*, "Transverter: Imbuing transformer-like properties in an interlink converter for robust control of a hybrid AC-DC microgrid," *IEEE Trans. Power Electron.*, vol. 34, no. 11, pp. 11332–11341, Nov. 2019.
- [5] S. Kenzelmann, A. Rufer, D. Dujic, F. Canales, and Y. R. de Novaes, "Isolated DC/DC structure based on modular multilevel converter," *IEEE Trans. Power Electron.*, vol. 30, no. 1, pp. 89–98, Jan. 2015.
- [6] X. Zhang, T. C. Green, and A. Junyent-Ferré, "A new resonant modular multilevel step-down DC-DC converter with inherent-balancing," *IEEE Trans. Power Electron.*, vol. 30, no. 1, pp. 78–88, Jan. 2015.
- [7] S. Debnath, J. Qin, B. Bahrani, M. Saeedifard, and P. Barbosa, "Operation, control, and applications of the modular multilevel converter: A review," *IEEE Trans. Power Electron.*, vol. 30, no. 1, pp. 37–53, Jan. 2015.
- [8] Y. Qiao, X. Zhang, X. Xiang, X. Yang, and T. C. Green, "Trapezoidal current modulation for bidirectional high-step-ratio modular DC-DC converters," *IEEE Trans. Power Electron.*, vol. 35, no. 4, pp. 3402–3415, Apr. 2020.
- [9] Y. Li, X. Lyu, and D. Cao, "A zero-current-switching high conversion ratio modular multilevel DC-DC converter," *IEEE J. Emerg. Sel. Topics Power Electron.*, vol. 5, no. 1, pp. 151–161, Mar. 2017.
- [10] X. Xiang, Y. Qiao, Y. Gu, X. Zhang, and T. C. Green, "Analysis and criterion for inherent balance capability in modular multilevel dc-ac-dc converters," *IEEE Trans. Power Electron.*, vol. 35, no. 6, pp. 5573–5580, Jun. 2020.
- [11] N. M. Wereley and S. R. Hall, "Frequency response of linear time-periodic systems," in *Proc. 29th IEEE Conf. Decis. Control*, Dec. 1990, vol. 6, pp. 3650–3655.
- [12] H. K. Khalil, *Nonlinear Systems*. Englewood Cliffs, NJ, USA: Prentice-Hall, 2002.
- [13] A. F. Bermant, *A Course of Mathematical Analysis: International Series of Monographs on Pure and Applied Mathematics*. New York, NY, USA: Elsevier, 2016.
- [14] P. Huang *et al.*, "Optimal design and implementation of high-voltage high-power silicon steel core medium-frequency transformer," *IEEE Trans. Ind. Electron.*, vol. 64, no. 6, pp. 4391–4401, Jun. 2017.
- [15] N. Soltau, H. Stagege, R. W. De Doncker, and O. Apeldoorn, "Development and demonstration of a medium-voltage high-power DC-DC converter for DC distribution systems," in *Proc. IEEE 5th Int. Symp. Power Electron. Distrib. Gener. Syst.*, 2014, pp. 1–8.